AI for Materials
https://www.sciltp.com/journals/aimat

Article

Supervised Machine Learning Assisted Development of Hybrid Solvation Model for Simulating Graphene-Water Interface

Jordan Clive Barker, William Wen and Yun Wang *

School of Environment and Science, Griffith University, Southport, QLD 4215, Australia
* Correspondence: yun.wang@griffith.edu.au

How To Cite: Barker, J.C.; Wen, W.; Wang, Y. Supervised Machine Learning Assisted Development of Hybrid Solvation Model for Simulating Graphene-Water Interface. *AI for Materials* **2025**, *1*(1), 3.

Received: 30 September 2025
Revised: 24 November 2025
Accepted: 24 November 2025
Published: 26 November 2025

Abstract: The electrified graphene-water interface is a vital component in many energy storage applications. However, understanding the interfacial properties is challenging due to the requirement of a high-quality atomic interfacial model. Recently, the hybrid solvation model, including the computationally affordable implicit solvation model and a thin layer of explicit water solvent slab next to the solid, has become a promising approach to address this issue. The identification of the rational explicit water slab thickness holds the key to the computational results by using this hybrid solvation model. In this study, we present a framework combining ab initio molecular dynamics (AIMD) and supervised machine learning (ML) to address this challenge. Based on the database from the AIMD simulations, the relationship between the total energy of the system and the distance from the oxygen in water molecules to the graphene was successfully identified through supervised ML. Our results further demonstrate that the first few layers of water next to the graphene play the decisive role in the change of the total energy. The cutoff thickness of 7 Å can reproduce the majority of the impact of the solvent on the total energy change of the water-graphene system. The success of this ML-assisted platform suggests it can also be used as a protocol to build the hybrid solvation model for understanding other electrified solid-liquid interfaces

Keywords: supervised machine learning; solid-liquid interface; graphene; AIMD; hybrid solvation model

1. Introduction

Graphene's remarkable properties, including exceptional electrical conductivity, large theoretical surface area, and superior mechanical strength, position it as a foundational material for next-generation technologies [1–12]. These attributes make it invaluable in energy storage, sensors, and electronics, with promise in supercapacitors. In electric double-layer capacitors (EDLCs), graphene's high conductivity, uniform pore distribution, and extensive surface exposure provide compact, efficient, and eco-friendly energy storage solutions with high power density and rapid charge/discharge rates [13–17]. The fundamental mechanism occurs at the electrified interface between graphene and the water solvent, where charge storage takes place [18]. Consequently, the graphene–water interface is of central importance, as it governs interfacial energetics, charge storage, and transfer. Accurate understanding of this interface is therefore essential for the rational design and optimisation of graphene-based electrochemical technologies, including supercapacitors and batteries.

Research on the graphene–water interface has progressed in three main directions. First, the explicit water solvation model is used to describe the interaction between the water molecules and graphene. Due to the dynamic nature of the water solvent under the mild working conditions, molecular dynamics (MD) has been used to offer

atomistic insights. The accurate ab initio MD (AIMD) has been used [17]. While it has been demonstrated to investigate the electrified interface, the AIMD computational cost is high [19]. The recent machine learning (ML) interatomic potentials have then replaced density functional theory (DFT) for MD simulations, greatly lowering computational cost while maintaining near first-principles accuracy [20]. However, such studies need the constant-potential MD on the electrified system, which are rarely reported. The second approach is to use the implicit solvation model. Implicit solvation model is a promising alternative by treating the solvent as a continuous, polarizable medium with a constant dielectric constant for efficiently simulating chemical and biological processes [21,22]. However, the recent studies demonstrate that the lack of explicit water molecules may lead to inaccurate interfacial properties [23]. To this end, hybrid approaches that combine both implicit and explicit solvation methods have become promising in addressing the shortcomings of these two solvation models [24]. The grand canonical DFT (GC-DFT) framework was introduced for this hybrid model, in which a single explicit water layer was retained to capture hydrogen bonding and interfacial orientation, while the surrounding solvent was treated implicitly, yielding improved predictions of interfacial properties such as the potential of zero charge [25]. Building on this foundation, Hinsch et al. applied the method to the Pt(111)/water interface, showing that an explicit bilayer with an implicit bulk reconciles calculated and experimental values of the potential of zero charge and double-layer capacitance [24]. More recently, Hinsch et al. extended this hybrid solvation model to Group 10 and 11 metals, confirming its accuracy and generality across different surfaces [26]. These studies highlight that the reduced number of waters plays a disproportionately important role at electrified interfaces, motivating the extension of hybrid solvation models to other systems such as graphene. However, a systematic means of quantifying which water layers must be retained explicitly remains lacking.

In this study, the supervised ML is employed to provide that guidance by quantifying the energetic role of water layers at the graphene-water interface. By using the AIMD results as a database, the supervised ML reveals the relationship between the total energy change of the system and the height of oxygen atoms of water in terms of the graphene monolayer. Our results highlight the dominant role of water next to the graphene in determining interfacial energetics, and the diminishing influence of subsequent layers that contribute only marginally.

2. AIMD Method

The Vienna Ab initio Simulation Package (VASP) was used for the AIMD simulation [27,28]. VASPkit was used to generate input files and data analysis [29]. The projected augmented wave (PAW) method was used to describe the valence wave function [30]. The valence configurations of C, H, and O atoms are $2s^2\ 2p^2$, $1s^2$, and $2s^2\ 2p^4$, respectively. The kinetic cut-off of 520 eV was used. Structural optimisation was performed until all Hellmann–Feynman forces were below 1×10^{-2} eV Å^{-1}, with electronic self-consistency achieved when the total energy change between successive iterations was less than 1×10^{-4} eV. Gamma-centred k-point meshes were generated with a reciprocal space resolution of $2\pi \times 0.04$ Å^{-1}. The optPBE non-localised van der Waals (vdW) functional was used for dispersion corrections [31].

Graphene, a two-dimensional material composed of carbon atoms in a honeycomb lattice, was chosen for this study due to its simple yet stable sp^2-hybridised structure [15,32,33]. The strong sp^2 C–C bonds contribute to its stability compared to sp^3-hybridised materials [34]. To simulate explicit solvation molecules, ab initio molecular dynamics (AIMD) was used, utilising a $(2\sqrt{3} \times 2\sqrt{3})$ R30° graphene supercell containing 24 carbon atoms with an area of 8.54 Å^2 and a depth of 30.0 Å. Water molecules were inserted into the vacant volume using Winmostar [35], with the number determined from the relation

$$N = \frac{V \cdot \rho \cdot N_A}{M}$$

where V is the simulation cell volume in cm^3, ρ is the water density (1 g·cm^{-3}), N_A is Avogadro's number, and M is the molar mass of water (18 g·mol^{-1}). This yielded 63 water molecules, corresponding to the experimental density of 1 g·mL^{-1}. With a timestep of 1 fs and a timescale of 1.4 ps, the AIMD computations were conducted at 350 K to simulate liquid-like behaviour, measured with Nosé-Hoover thermostat [36–39]. Additional calculations up to the timescale of 19.5 ps were performed to justify the AIMD simulation timescale used in this study.

3. Supervised ML Method

The supervised ML model was implemented using PyTorch and trained using the Adam optimiser [40,41]. Input features were constructed from the atomic trajectory from the AIMD simulations, where per-frame atomic positions of oxygen relative to graphene were extracted. For each oxygen atom, the distances to all carbon atoms were calculated, and the absolute displacement from the median graphene plane (Δz) was also computed. These

two input features were used as inputs to a feed-forward neural network. A Δz cutoff of 5.0, 6.0, 7.0, or 8.0 Å was applied, excluding water further from the graphene plane to focus the model on interfacial interactions.

The model consisted of a fully connected network with two hidden layers of 64 neurons each, using the SiLU activation function. The network produced per-oxygen contributions, which were summed to predict the total frame energy. Training labels were obtained from total energies of the AIMD simulations. Hereafter, 'total energy' denotes E_0. A mean-squared error (MSE) loss function was used, with an optional stabilisation penalty term weighted by Δz.

Out of 1400 frames, the first 200 were trimmed to remove since their energy are not converged. After the structure reaches the optimised configuration, as evidenced by the stabilised total energy, the remaining 1200 frames were randomly split into training (80%) and validation (20%) with a fixed seed for reproducibility. During training, checkpoints were saved on validation-loss improvement.

4. Results and Discussion

Figure 1a shows the initial configuration generated by using Winmostar with the water density of 1 g cm^{-3}. It can be found that some water molecules are far from the graphene, which indicates that this atomic structure is unstable. The unstable interface configuration can be stabilized through the AIMD simulation. One snapshot of the stabilized graphene-water interface structure is shown in Figure 1b. The stability was evaluated based on the energy fluctuation over the AIMD simulation time. From Figure 1c, it can be found that the initial energy is about 100 eV higher than the stabilized energy after a 200-fs timeframe. It supports the instability of this initial structure. After the 200 fs, the energy fluctuation becomes small. Consequently, we use the total energies from 200 to 1400 fs time frames and the corresponding atomic coordinates for the supervised ML. Figure 1d indicates the different water densities in relation to the graphene using the C–O radial distribution function (RDF). The first layer forms between 3.0 to 5.0 Å, and the second layer between 6.0 to 8.0 Å. Hence, we use 5.0, 6.0, 7.0, and 8.0 Å to represent the full interfacial layer to the inclusion of the second layer. Additionally, the changes of the total energies are small after 1.4 ps (see Figure 1c); and the C–O RDF images are almost identical for the MD simulations with 1.4 and 19.5 ps timescales (see Figure 1d). It demonstrates that the 1.4 ps timescale is long enough for this study, which can be largely attributed to the weak water-graphene interaction strength [17].

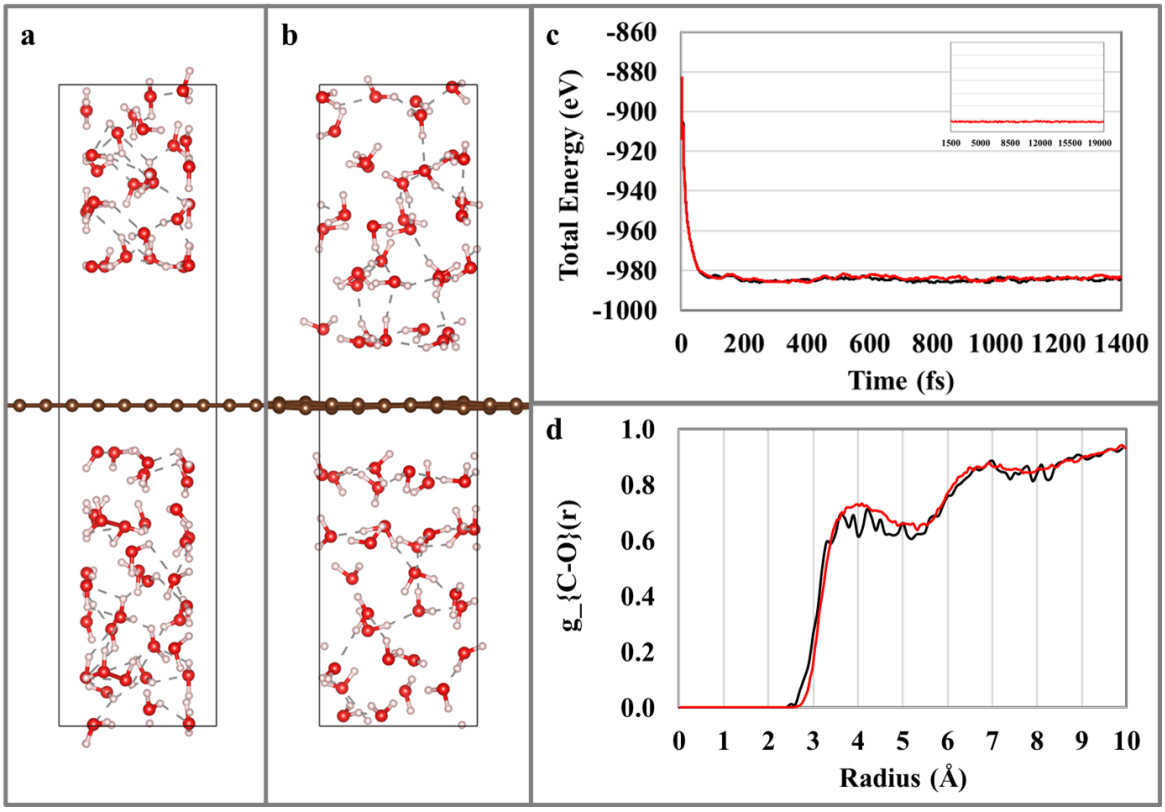

Figure 1. (**a**) Initial atomic graphene-water interface structure for the AIMD simulation, (**b**) one snapshot of atomic graphene-water interface structure when the total energy is stabilised during the AIMD simulation, (**c**) plot of total energy fluctuation of the graphene-water interfaces over time and (**d**) radial distribution function (RDF) plot for AIMD with the timescales of 1.4 ps (black) and 19.5 ps (red). Colour code: brown-C, red-O, and pink-H.

Theoretically, the total energy of a system is determined by all the interatomic forces, which are often described by the force field parameters in classical MD simulations. However, previous studies reveal that the graphene monolayer is hydrophobic [17]. As a result, the interaction between graphene and water is mainly by the van der Waals (vdW) force, which is largely determined by the distance between the water molecules and the graphene. On the other hand, the water-water interaction is determined by the intermolecular hydrogen bonds, which would not be affected by the vdW interaction between water and graphene at the interface [17]. In this context, the total energy change of the graphene-water interface may be mainly determined by the distance between water molecules and the graphene monolayer. More specifically, the vertical distance between the oxygen atoms in water molecules and the graphene monolayer (Δz) can be strongly relevant to the total energy of the interface. To this end, the ML is used to identify the relationship between the distance and the total energy of the graphene-water interface.

After removing the unstable states of the AIMD data in the first 200 timeframe steps, the kernel density estimates (KDE) were first generated through the supervised ML, as shown in the left panels of Figure 2. A KDE is a non-parametric way to estimate the probability density function of a random variable. It visualizes the distribution of data points, with higher density areas appearing darker or more concentrated. Our KDE plots show the relationship between the distribution of the total energy in per-water contributions at the specific Δz. The distribution of the total energy (E_{tot}) is calculated based on the sum of per-water contribution energy over the simulation time, as shown below:

$$E_{tot} = \sum_{i,j} E_{ij}(d, \Delta z)$$

where i is the timestep and the E_i is the energy distribution at that specific timestep, and j is the specific oxygen-carbon relation for distance (d) and Δz.

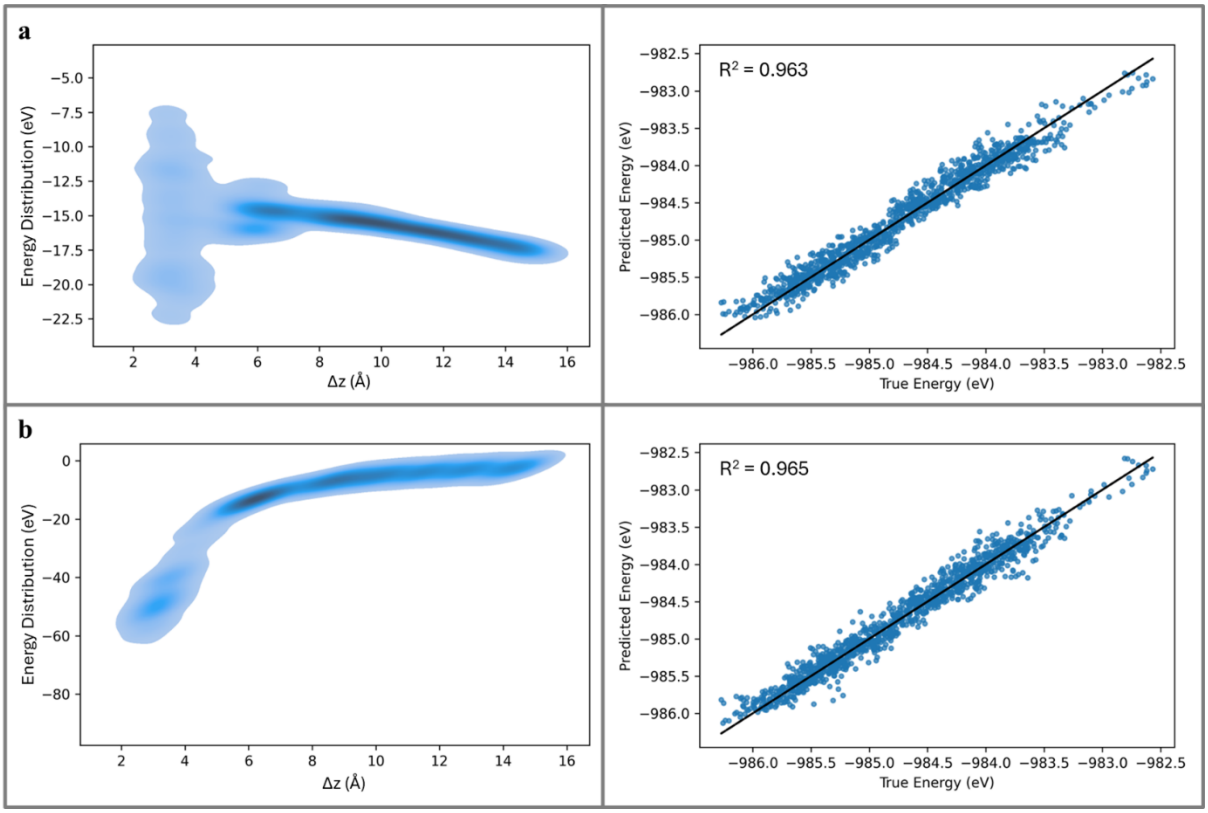

Figure 2. Left: Kernel density estimates showing the relation between energy (eV) and Δz (Å) for oxygen atoms of water molecules under (**a**) unweighted and (**b**) weighted training. Right: predicted versus true total energies for the corresponding models.

Two training strategies were adopted. In the unweighted approach, the model was trained solely by minimising the MSE between the predicted and reference total energies (E_0):

$$L_{unweighted} = MSE(E_d, E_0)$$

To further emphasise the energetic role of water slabs closer to the graphene, a weighted approach was applied. Here, a quadratic penalty on the Δz and predicted per-oxygen energy was added to the loss, discouraging large contributions from distant solvents.

$$L_{weighted} = MSE(E_d, E_0) + \frac{\lambda}{N}\sum_{i=1}^{N}(E_i \times \Delta z)^2$$

where λ is the weighting factor (1×10^{-3}) and N is the number of water molecules

The top left plot (a) shows the KDE for unweighted training, where each data point representing a specific state of the graphene-water system is treated with equal importance. The data forms a tight, narrow distribution. This suggests that the model, trained on all states equally, identifies a relatively consistent relationship, in which the energy distribution becomes less negative as Δz increases. This indicates that the interaction between water and graphene weakens. This KDE based on the unweighted training model suggests a strong probability peak at approximately −15 eV, corresponding to a Δz of about 10 Å.

The bottom left plot (b) shows the KDE for weighted training. This weighted training method assigns greater importance to the data points with smaller Δz. In this case, the weighted training results in a much broader and more diffuse KDE distribution. The energy distribution spans a wider range, particularly at smaller Δz values, where the plot shows a much steeper and more dramatic change in energy contribution. This suggests that weighting the training data reveals a more complex and varied energy landscape, capturing more extreme or nuanced interactions that were less apparent in the unweighted model. The stark difference between the two plots highlights how the training method significantly influences what the ML model learns about the underlying physics of the graphene-water interface. Without weighting, the interfacial water layer exhibited the greatest variability, with oxygen atoms contributing either strongly or weakly to the total energy. By contrast, the second and bulk layers produced smoother distributions, with the bulk showing a consistently higher contribution than the second layer. It suggests that the bulk is more stable than the water slabs with a Δz less than 8 Å. When weighting was applied so that the first layer contributed most and the furthest the least, the KDE curve stabilised while shifting to favour the first hydration layer. However, both results demonstrate a clear distance-dependent trend that the water molecules closer to the graphene provide the dominant energetic contribution to the interface systems.

Based on the KDE results, the total energies of the systems were recalculated only based on the Δz values of all oxygen atoms in water molecules, which are shown in the right panels of Figure 2. Although the unweighted and weighted approaches produced different KDE plots, both reproduced the total energies with high accuracy, achieving a minimum R^2 of 0.96. This confirmed a consistent relationship between energy and distance across the system.

Next, to identify the minimum explicit water slab thickness needed for building hybrid solvation models, we used supervised ML to retrain the model by only including Δz values of 5.0, 6.0, 7.0, or 8.0 Å of the oxygen atoms in water modules. Figure 3 shows the corresponding KDE plots using the unweighted training method. Its predictive accuracy was evaluated by comparing the predicted energy against the true energy, quantified by the coefficient of determination (R^2). Initially, a Δz cutoff of 5.0 Å yielded an R^2 of 0.86, indicating a modest correlation. Increasing the cutoff to 6.0 Å resulted in a substantial performance improvement, with the R^2 value rising to 0.96. This significant jump suggests that including water molecules up to this distance is critical for the model to accurately capture the key energetic interactions. Further increasing the cutoff to 7.0 Å and 8.0 Å led to only marginal changes in the R^2 values (0.95 and 0.96, respectively). This finding indicates that the predictive power of the ML based on the unweighted training model plateaus beyond a Δz cutoff of approximately 6.0 Å. The diminishing returns in predictive accuracy suggest that the energetic contributions from water molecules further away from the graphene surface are either minimal or are adequately represented by the model trained on a 6.0 Å slab. Therefore, a Δz of 6.0 Å represents an optimal balance between computational efficiency and predictive fidelity for this system.

In contrast, the weighted training method (see Figure 4) assigns greater importance to certain data points, which are likely those that represent energetically distinct or critical configurations. Table 1 lists the different R^2 values for two training methods with different cutoff Δz values. The unweighted model shows a dramatic jump in accuracy from a Δz of 5.0 Å to 6.0 Å, indicating a clear threshold, where including the water with smaller Δz values than 6.0 Å becomes critical for accurate prediction. The weighted model, however, shows a more gradual increase in accuracy as the water slab thickness increases. While the unweighted model achieves a higher R^2 at the 6.0 Å cutoff, the weighted model consistently improves as more data is included, reaching a final R^2 of 0.955 at 8.0 Å, which is comparable to the unweighted model.

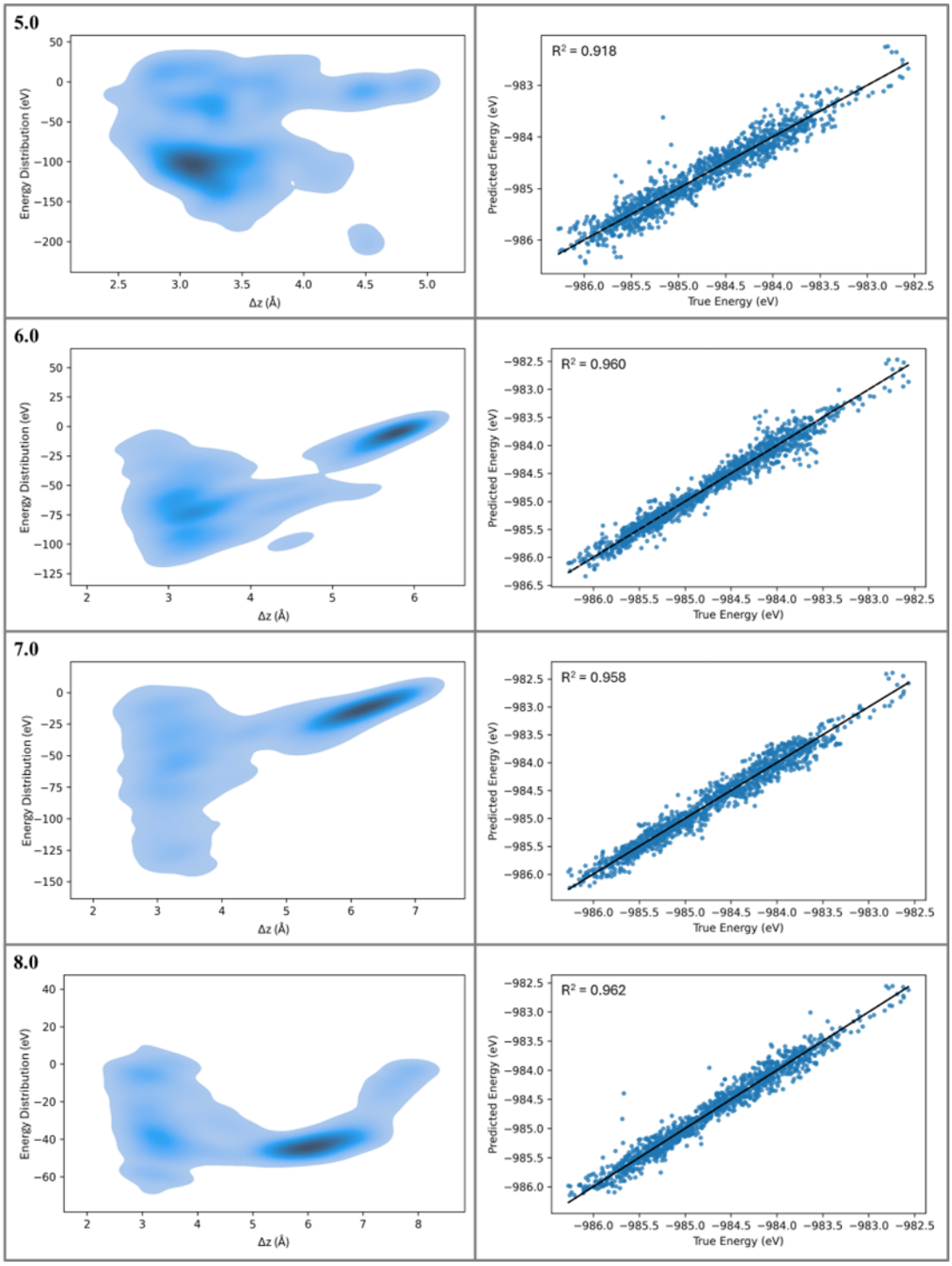

Figure 3. The **left** panels show kernel density estimates for the relation between energy distribution (eV) and Δ*z* (Å) for oxygen atoms under unweighed training with Δ*z* cutoffs of 5.0, 6.0, 7.0, and 8.0 Å. The **right** panels show predicted versus true total frame energies for the corresponding models.

Table 1. Comparison of the R^2 values for the unweighted and weighted training methods.

Δz (Å)	R^2 (Unweighted Training)	R^2 (Weighted Training)
5.0	0.918	0.879
6.0	0.960	0.910
7.0	0.958	0.948
8.0	0.962	0.955

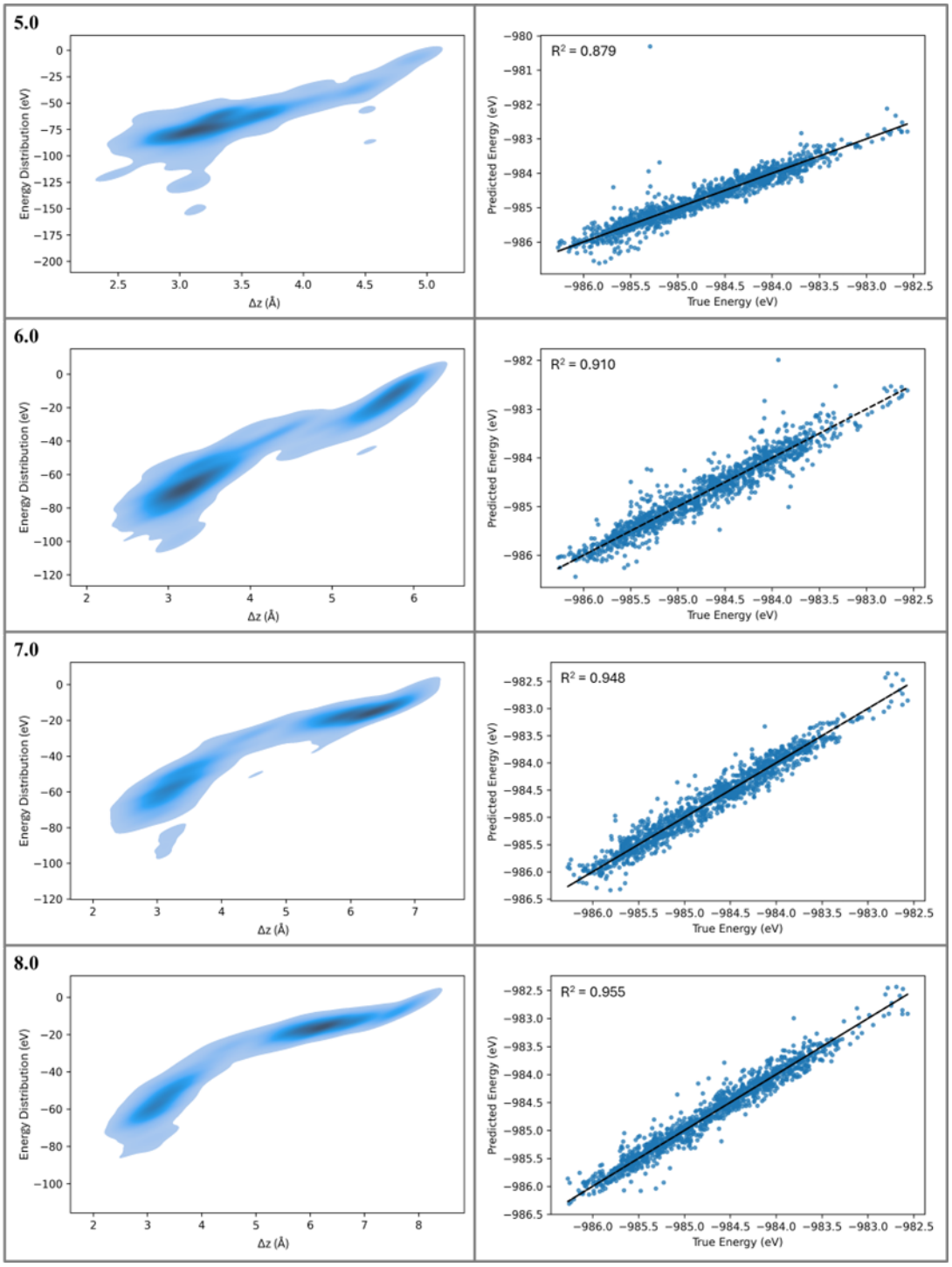

Figure 4. Kernel density estimates showing the relation between energy contribution (eV) and Δ*z* (Å) for oxygen atoms under weighted training with Δ*z* cutoffs of 5.0, 6.0, 7.0, and 8.0 Å. The right panels show predicted versus true total frame energies for the corresponding models.

This suggests a fundamental difference in how the two models learn. The unweighted model identifies a critical water slab thickness, where the key interactions are fully captured, leading to a rapid convergence in accuracy. The weighted model, on the other hand, learns from a more diverse set of data and continues to refine its predictions as more information is added, eventually catching up to and potentially surpassing the unweighted model's performance at larger thicknesses. The weighted training method thus provides a more robust and less sensitive approach to determining the required explicit water thickness, as its performance improves more predictably with the inclusion of additional data.

Figure 5 provides a visual representation of the atomic structures for the graphene-water interface at different cutoff Δ*z* values. Each panel illustrates the system with increasing water slab thickness, corresponding to the 5 Å, 6 Å, 7 Å, and 8 Å cutoffs used in the ML models. It is clearly shown that as the cutoff distance increases, additional

layers of water molecules are included in the simulation box. The 5 Å cutoff includes only the first layer of water directly interacting with the graphene. The 7 Å cutoff includes a second layer of water. At 8 Å, the system contains multiple, more complex layers, including those that begin to resemble the bulk-like behaviour of liquid water away from the interface.

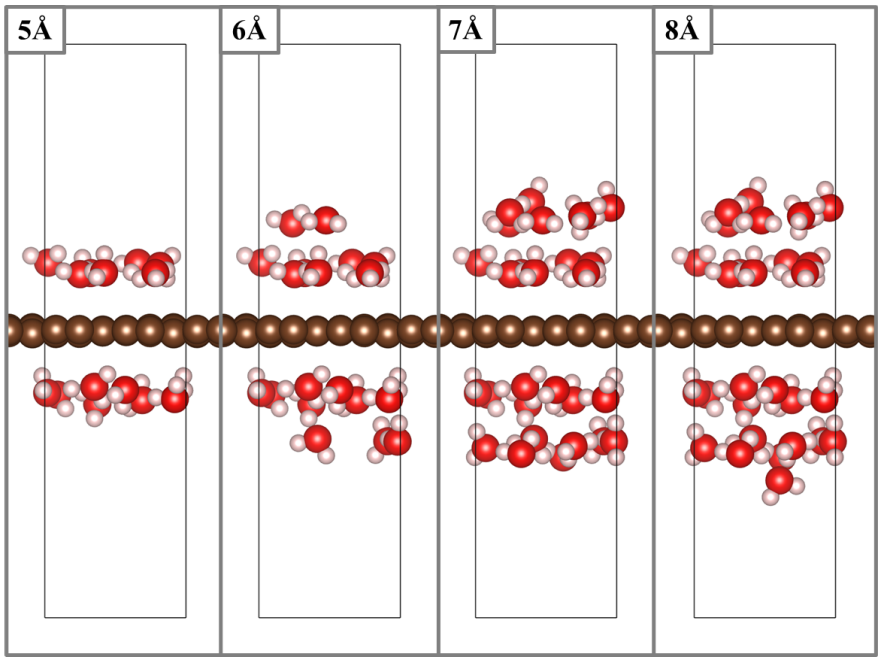

Figure 5. Snapshot of final configuration of graphene-water interface at varying cutoff distances, showing 5 Å with interfacial layer, 6 Å showing partial second layer, 7 Å with both first and second layer, and 8 Å with partial bulk layer.

Combining this structural information with the ML model performance from the other figures yields significant insights. The unweighted training model demonstrates a substantial increase in predictive accuracy (R^2 increases from 0.861 to 0.960) when the cutoff is increased from 5 Å to 6 Å. This can be directly attributed to the inclusion of the second water layer, as shown in Figure 5. This layer is crucial for establishing the hydrogen bond network and more accurately representing the total energy of the system. The failure to perform well at 5 Å is because it lacks information about these critical intermolecular hydrogen bonds [17].

The weighted training model also supports the importance of including the second layer of water to accurately describe the graphene-water interface. However, it shows a more gradual improvement in accuracy. This suggests that the weighted model is better at learning the complex interactions within a single layer and is less dependent on the full structural context provided by the additional layers. Ultimately, Figure 5 provides the physical context that explains the observed trends in model performance, demonstrating that a minimum explicit water thickness of 7 Å, corresponding to the inclusion of the first two water layers next to the graphene, is essential for accurate energetic modelling of the graphene-water interface.

5. Conclusions

In this study, we employed DFT-based AIMD simulations to build a database including the change of the total energy of the graphene-water interface and the Δz values of oxygen atoms in water molecules. By using the database from the AIMD simulations, the supervised ML was served as a tool to decompose these energies and quantify the role of different water layers. Regardless of the weighting scheme or cutoff distance, the first hydration layer consistently dominated the interfacial energetics, whereas the bulk layers were marginal. These findings demonstrate that explicit treatment of the first and second layer with the Δz value of 7 Å, coupled with implicit treatment of the remaining solvent, provides a computationally efficient yet physically accurate framework for modelling graphene–water interfaces. This study, therefore, establishes that the essential physics of the graphene–water interface are captured. It can also provide the foundation for building a hybrid solvation model for understanding other electrified solid-liquid interface properties.

Author Contributions

J.C.B.: methodology, software, data curation, writing—original draft preparation, visualization, investigation, validation; W.W.: writing—reviewing and editing; Y.W.: conceptualization, supervision, writing—reviewing and editing. All authors have read and agreed to the published version of the manuscript.

Funding

This research was funded by the Australian Research Council Discovery Project, grant number: DP210104010, and also by the National Computational Infrastructure (NCI), grant number: p74.

Institutional Review Board Statement

Not applicable.

Informed Consent Statement

Not applicable.

Data Availability Statement

The data that support the findings of this study are available from the corresponding author, Y.W., upon reasonable request.

Acknowledgments

The authors acknowledge financial support from the Australian Research Council Discovery Project (Grant No. DP210104010). This research was undertaken on the supercomputers in the National Computational Infrastructure (NCI) in Canberra, Australia, which is supported by the Australian Commonwealth Government, and the Pawsey Supercomputing Centre in Perth, with funding from the Australian Government and the Government of Western Australia.

Conflicts of Interest

The authors declare no conflict of interest.

Use of AI and AI-Assisted Technologies

During the preparation of this work, the authors used AI tools to assist in technical and editorial works for refining, improving clarity, and exploring technical solutions, while all core developments were done by the authors. After using this tool/service, the authors reviewed and edited the content as needed and take full responsibility for the content of the published article.

References

1. Ray, S.C. *Applications of Graphene and Graphene-Oxide Based Nanomaterials*; William Andrew Publishing: Norwich, NY, USA, 2015. https://doi.org/10.1016/C2014-0-02615-9.
2. Wang, X.; Zhi, L.; Müllen, K. Transparent, Conductive Graphene Electrodes for Dye-Sensitized Solar Cells. *Nano Lett.* **2008**, *8*, 323–327. https://doi.org/10.1021/nl072838r.
3. Balandin, A.A.; Ghosh, S.; Bao, W.; et al. Superior Thermal Conductivity of Single-Layer Graphene. *Nano Lett.* **2008**, *8*, 902–907. https://doi.org/10.1021/nl0731872.
4. Kim, T.Y.; Park, C.-H.; Marzari, N. The Electronic Thermal Conductivity of Graphene. *Nano Lett.* **2016**, *16*, 2439–2443. https://doi.org/10.1021/acs.nanolett.5b05288.
5. Yavari, F.; Koratkar, N. Graphene-Based Chemical Sensors. *J. Phys. Chem. Lett.* **2012**, *3*, 1746–1753. https://doi.org/10.1021/jz300358t.
6. Hill, E.W.; Vijayaragahvan, A.; Novoselov, K. Graphene Sensors. *IEEE Sens. J.* **2011**, *11*, 3161–3170. https://doi.org/10.1109/JSEN.2011.2167608.
7. Zhou, Y.; Bao, Q.; Tang, L.A.L.; et al. Hydrothermal Dehydration for the “Green” Reduction of Exfoliated Graphene Oxide to Graphene and Demonstration of Tunable Optical Limiting Properties. *Chem. Mater.* **2009**, *21*, 2950–2956. https://doi.org/10.1021/cm9006603.

8. Huang, C.; Li, C.; Shi, G. Graphene based catalysts. *Energy Environ. Sci.* **2012**, *5*, 8848–8868. https://doi.org/10.1039/C2EE22238H
9. Julkapli, N.M.; Bagheri, S. Graphene supported heterogeneous catalysts: An overview. *Int. J. Hydrogen Energy* **2015**, *40*, 948–979. https://doi.org/10.1016/j.ijhydene.2014.10.129.
10. Falkovsky, L.A. Optical properties of graphene. *J. Phys. Conf. Ser.* **2008**, *129*, 012004. https://doi.org/10.1088/1742-6596/129/1/012004.
11. Shao, Y.; El-Kady, M.F.; Wang, L.J.; et al. Graphene-based materials for flexible supercapacitors. *Chem. Soc. Rev.* **2015**, *44*, 3639–3665. https://doi.org/10.1039/C4CS00316K.
12. Nag, A.; Mitra, A.; Mukhopadhyay, S.C. Graphene and its sensor-based applications: A review. *Sens. Actuators A Phys.* **2018**, *270*, 177–194. https://doi.org/10.1016/j.sna.2017.12.028.
13. Ghosh, S.; Barg, S.; Jeong, S.M.; et al. Heteroatom-Doped and Oxygen-Functionalized Nanocarbons for High-Performance Supercapacitors. *Adv. Energy Mater.* **2020**, *10*, 2001239. https://doi.org/10.1002/aenm.202001239.
14. Park, S.; Ruoff, R.S. Chemical methods for the production of graphenes. *Nat. Nanotechnol.* **2009**, *4*, 217–224. https://doi.org/10.1038/nnano.2009.58.
15. Ke, Q.; Wang, J. Graphene-based materials for supercapacitor electrodes—A review. *J. Mater.* **2016**, *2*, 37–54. https://doi.org/10.1016/j.jmat.2016.01.001.
16. Huang, S.; Zhu, X.; Sarkar, S.; et al. Challenges and opportunities for supercapacitors. *APL Mater.* **2019**, *7*, 100901. https://doi.org/10.1063/1.5116146.
17. Akaishi, A.; Yonemaru, T.; Nakamura, J. Formation of Water Layers on Graphene Surfaces. *ACS Omega* **2017**, *2*, 2184–2190. https://doi.org/10.1021/acsomega.7b00365.
18. Wang, Y.; Tang, F.; Yu, X.; et al. Heterodyne-Detected Sum-Frequency Generation Vibrational Spectroscopy Reveals Aqueous Molecular Structure at the Suspended Graphene/Water Interface. *Angew. Chem. Int. Ed.* **2024**, *63*, e202319503. https://doi.org/10.1002/anie.202319503.
19. Bouzid, A.; Gono, P.; Pasquarello, A. Reaction pathway of oxygen evolution on Pt(111) revealed through constant Fermi level molecular dynamics. *J. Catal.* **2019**, *375*, 135–139.
20. Noordhoek, K.; Bartel, C.J. Accelerating the prediction of inorganic surfaces with machine learning interatomic potentials. *Nanoscale* **2024**, *16*, 6365–6382. https://doi.org/10.1039/D3NR06468A.
21. Islam, S.M.R.; Khezeli, F.; Ringe, S.; et al. An implicit electrolyte model for plane wave density functional theory exhibiting nonlinear response and a nonlocal cavity definition. *J. Chem. Phys.* **2023**, *159*, 234117. https://doi.org/10.1063/5.0176308.
22. Mathew, K.; Kolluru, V.S.C.; Mula, S.; et al. Implicit self-consistent electrolyte model in plane-wave density-functional theory. *J. Chem. Phys.* **2019**, *151*, 234101. https://doi.org/10.1063/1.5132354.
23. Ringe, S.; Hörmann, N.G.; Oberhofer, H.; et al. Implicit Solvation Methods for Catalysis at Electrified Interfaces. *Chem. Rev.* **2022**, *122*, 10777–10820. https://doi.org/10.1021/acs.chemrev.1c00675.
24. Hinsch, J.J.; Bouzid, A.; Barker, J.C.; et al. Revisiting the Electrified Pt(111)/Water Interfaces through an Affordable Double-Reference Ab Initio Approach. *J. Phys. Chem. C* **2023**, *127*, 19857–19866. https://doi.org/10.1021/acs.jpcc.3c05425.
25. Xu, P.; von Rueden, A.D.; Schimmenti, R.; et al. Optical method for quantifying the potential of zero charge at the platinum–water electrochemical interface. *Nat. Mater.* **2023**, *22*, 503–510. https://doi.org/10.1038/s41563-023-01474-8.
26. Hinsch, J.J.; White, J.J.; Wang, Y. Theoretical investigation on potential of zero free charge of (111) and (100) surfaces of Group 10 and 11 metals. *Comput. Theor. Chem.* **2024**, *1232*, 114462. https://doi.org/10.1016/j.comptc.2024.114462.
27. Kresse, G.; Furthmüller, J. Efficiency of ab-initio total energy calculations for metals and semiconductors using a plane-wave basis set. *Comput. Mater. Sci.* **1996**, *6*, 15–50. https://doi.org/10.1016/0927-0256(96)00008-0.
28. Kresse, G.; Furthmüller, J. Efficient iterative schemes for ab initio total-energy calculations using a plane-wave basis set. *Phys. Rev. B* **1996**, *54*, 11169–11186. https://doi.org/10.1103/PhysRevB.54.11169.
29. Wang, V.; Xu, N.; Liu, J.-C.; et al. VASPKIT: A user-friendly interface facilitating high-throughput computing and analysis using VASP code. *Comput. Phys. Commun.* **2021**, *267*, 108033. https://doi.org/10.1016/j.cpc.2021.108033.
30. Kresse, G.; Joubert, D. From ultrasoft pseudopotentials to the projector augmented-wave method. *Phys. Rev. B* **1999**, *59*, 1758–1775. https://doi.org/10.1103/PhysRevB.59.1758.
31. Klimeš, J.; Bowler, D.R.; Michaelides, A. Chemical accuracy for the van der Waals density functional. *J. Phys. Condens. Matter* **2010**, *22*, 022201. https://doi.org/10.1088/0953-8984/22/2/022201.
32. Yang, W.; Ni, M.; Ren, X.; et al. Graphene in Supercapacitor Applications. *Curr. Opin. Colloid Interface Sci.* **2015**, *20*, 416–428. https://doi.org/10.1016/j.cocis.2015.10.009.
33. Tan, Y.B.; Lee, J.-M. Graphene for supercapacitor applications. *J. Mater. Chem. A* **2013**, *1*, 14814–14843. https://doi.org/10.1039/C3TA12193C.
34. Papageorgiou, D.G.; Kinloch, I.A.; Young, R.J. Mechanical properties of graphene and graphene-based nanocomposites. *Prog. Mater. Sci.* **2017**, *90*, 75–127. https://doi.org/10.1016/j.pmatsci.2017.07.004.
35. X-Ability Co., Ltd. *Winmostar V11.13.2*; X-Ability Co., Ltd.: Tokyo, Japan, 2025.

36. Mortier, F.; Zhao, D.; Otani, M.; et al. First-principles investigation of electrified monolayered MoS_2/water interface. *Surf. Sci.* **2026**, *764*, 122870. https://doi.org/10.1016/j.susc.2025.122870.
37. VandeVondele, J.; Mohamed, F.; Krack, M.; et al. The influence of temperature and density functional models in ab initio molecular dynamics simulation of liquid water. *J. Chem. Phys.* **2004**, *122*, 014515. https://doi.org/10.1063/1.1828433.
38. Sit, P.H.L.; Marzari, N. Static and dynamical properties of heavy water at ambient conditions from first-principles molecular dynamics. *J. Chem. Phys.* **2005**, *122*, 204510. https://doi.org/10.1063/1.1908913.
39. Soper, A.K. *Water and Ice Structure in the Range 220—365 K from Radiation Total Scattering Experiments*; IOS Press: Amsterdam, The Netherlands, 2014. https://doi.org/10.3254/978-1-61499-507-4-151.
40. Paszke, A.; Gross, S.; Chintala, S.; et al. *Automatic Differentiation in PyTorch*; NIPS-W: San Diego, CA, USA, 2017.
41. Kingma, D.P.; Ba, J. Adam: A Method for Stochastic Optimization. *arXiv* **2014**, arXiv:1412.6980.